Shuttle Orbiter Re-Entry Flowfields at High Angle of Attack

WILLIAM C. ROCHELLE*
Lockheed Electronics Co., Houston, Texas
BARNEY B. ROBERTS†
NASA/Johnson Spacecraft Center, Houston, Texas
AND
LEO D'ATTORRE‡ AND M. A. BILYK§
TRW Systems, Redondo Beach, Calif.

An analysis of the continuum inviscid and boundary-layer flowfields around various configurations representative of an early version of a space shuttle orbiter re-entering the atmosphere at 40° and 60° angle of attack is presented. The inviscid flow fields were predicted by 2-D time-dependent and 3-D steady finite difference/artificial viscosity techniques, together with a 2-D shock layer analysis method. Boundary-layer flow and heating rates were computed with an integral matrix technique. Configurations which were considered in the analysis included: 1) 2-D flat plate representations of the flat underside of the orbiter fuselage, 2) 2-D orbiter fuselage cross sections, 3) 2-D orbiter wing airfoils, and 4) a 3-D straight-wing orbiter configuration. Theoretical results correlated satisfactorily with pressure and heat transfer data on flat plates and wings (including shock intersection regions).

Nomenclature

c = speed of sound
C_H = heat transfer coefficient
C^* = viscosity parameter
D_λ = dissipative coefficient
E = internal energy
F_i = flow variables defined by Eqs. (4) and (7)
$F1_i$ = $f(W1_j)$
$F2_i$ = $f(W2_j)$
G_i = flow variables defined by Eqs. (4) and (7)
$G3_i$ = $f(W3_j)$
$G4_i$ = $f(W4_j)$
h = coordinate vector
H = static enthalpy; also altitude
L = plate length
M_∞ = Mach no.
p = pressure
P_{stag} = stagnation pressure
q_C = heat transfer rate along centerline
q_{fs} = heat transfer rate for freestream conditions
q_w = heat transfer rate to wall
$q_{w_{sph,r=1}}$ = heat transfer rate to wall for 1 ft radius sphere
Q_i = flow variables defined by Eq. (5)
r = radial coordinate
Re_x = Reynolds no. based on length, x
r = radial coordinate
S/B = lateral/chine line distance ratio defined in Fig. 5
t = time
u = velocity in x (or z) direction
v = velocity in y (or r) direction
w = velocity in z direction
W_i = flow variables defined by Eqs. (4) and (7)
$W1_j$ etc. = flow variables at the middle step
x, y, z = dimensional coordinates of orbiter surfaces
α = angle of attack; also time or x coordinate
β = z or y coordinate
γ = ratio of specific heats; also r or z coordinate
Γ = stability parameter in Eq. (13)
ε = total enthalpy
θ = flow angle
λ_1, λ_2 = quantities in Eq. (11)
μ = arctan $(M_\infty^2 - 1)^{-1/2}$
ρ = density

Presented as Paper 72-314 at the AIAA 7th Thermophysics Conference, San Antonio, Texas, April 10-12, 1972; submitted January 26, 1973; revision received August 15, 1973. This investigation was sponsored by NASA/JSC, Houston, Texas, under contract NAS 9-11207. The authors wish to acknowledge the technical assistance of A. V. Gomez, formerly of TRW Systems, Houston, Texas and now of Aerotherm Corporation, Mountain View, California.

Index categories: Supersonic and Hypersonic Flow; Boundary Layers and Convective Heat Transfer—Laminar; Bounday Layers and Convective Heat Transfer—Turbulent.

* Principal Engineer; formerly Member of Professional Staff, TRW Systems, Houston, Texas.
† Aerospace Engineer, Engineering Analysis Division.
‡ Member of Professional Staff. Member AIAA.
§ Member of Professional Staff.

Introduction

THE NASA space shuttle vehicle is being designed as a low cost, partially resuable space transportation system capable of ferrying men and equipment to space, deploying and/or repairing satellites, and so on, and returning to earth at moderately high angles of attack. The configuration on which this aerothermal analysis was based was an early straight-wing orbiter which was designed to enter the atmosphere at high angle of attack (40°–60°). This high angle of attack would produce a low cross range capability but would minimize the total heat load on the vehicle.

An adequate design of the orbiter structure and thermal protection system requires that the re-entry flowfield and thermal environment around the vehicle be accurately determined. In the past two years various orbiter re-entry aerothermodynamic analysis have been performed.[1–3] The re-entry aerothermal study[4,5] summarized in this paper was performed for both the rarefied and continuum flow regimes. The high altitude, rarefied flow portion of the orbiter analysis was presented previously.[6,7]

This paper presents the results of the lower altitude, continuum inviscid and boundary-layer flowfield analysis as outlined in Table 1. The physical model used to simulate the orbiter was based upon four basic shapes or configurations: 1) flat plates which represented either the flat underside of the orbiter fuselage of length 120 ft or a flat plate at $\alpha = 60°$ on which experimental data was measured; 2) a 2-D orbiter cross section at $\alpha = 60°$, composed of a flat bottom, sides at right angles to the bottom, and a semicircular top tangent to the sides; 3) 2-D orbiter wing airfoils (NACA 0012-64) at $\alpha = 40°$ and 60°, and 4) a 3-D pointed cone nose representation of the orbiter fuselage at $\alpha = 40°$ (with sharp-edged slab wings) which had the exact orbiter fuselage contours aft of the conical nose.

Table 1 List of inviscid flowfield cases analyzed by finite difference and shock layer techniques

No.	Type[c]	Alt. (KFt)	α(°)	M_∞	γ[b]
a) *2-D flat plate cases*[a]					
1	*FD*	195	60	13.7	1.4
2	*FD*	195	60	13.7	var.
3	*FD*	289	60	20	1.4
4	*FD*	289	60	20	var.
5	*FD*	269	60	28.3	1.4
b) *2-D orbiter fuselage cross section case*					
1	*FD*	269	60	28.3	1.4
c) *2-D orbiter wing airfoil cases*					
1	*SL*	269	60	28.3	1.4
2	*SL*	250	40	26.65	1.4
d) *3-D orbiter fuselage/wing case*					
1	*FD*	250	40	26.65	1.4

[a] Cases 1, 2, and 5 represent the bottom of the orbiter fuselage, while cases 3 and 4 represent a flat plate at $\alpha = 60°$ tested at CAL.
[b] $\gamma = 1.4$ denotes ideal gas, while γ = variable denotes real gas.
[c] *FD* = finite difference programs, *SL* = shock layer program.
Note: BLIMP program used for boundary-layer analysis based on above inviscid analyses.

Two of the cases listed in Table 1 considered real gas (variable γ) effects while the others involved an ideal gas ($\alpha = 1.4$) analysis. For each of the cases the boundary-layer flow and heating rates were computed using the inviscid flow surface pressure distributions as input. The combined results of the finite difference, airfoil shock layer, and heating analysis were used to determine the fuselage shock/wing shock intersection region on the wing leading edge. All calculations were performed for points on either an $\alpha = 60°$ trajectory[8] or an $\alpha = 45°$ trajectory[9] (on which the $\alpha = 40°$ calculations were based).

In the following sections the general theory of the finite difference/artificial viscosity technique is described in detail as it applies to the configurations investigated. The shock layer inviscid flowfield method is briefly discussed as is the boundary layer flow and heating analysis. A presentation of shock location, surface pressure, and heating rate results is given as compared with test data[10–22] listed in Table 2.

Analysis

Finite Difference Inviscid Flowfield

Since a 3-D time-dependent finite difference method for arbitrary shaped, blunt-nosed bodies at high α was not available (with a reasonable computer run time), it was necessary to perform an "approximate" type of 3-D flow calculation for various parts of the orbiter. In Ref. 23 the justification for such flowfield approximations for 3-D bodies is given, along with a survey of these methods as applied to windward surfaces of hypersonic lifting bodies at high α. If the aspect ratio is large enough (such as for the bottom of the orbiter) the flow locally approaches a 2-D flow, independent of the actual value of the aspect ratio, and methods such as the "strip theory" concept[23] or 2-D time-dependent finite difference methods may be used to approximate the flow around 3-D shapes. In addition, if the blunt nose region of a lifting body is small compared to the rest of the body (such as the orbiter) the body can be assumed to have a pointed nose with attached shock and the entire supersonic flowfield may be computed by a steady, marching 3-D finite difference technique.

For the present study, the inviscid flowfields along flat plates representing the underside of the orbiter at $\alpha = 60°$ (where the shock was detached) were computed by a 2-D time-dependent finite difference/artificial viscosity approach. The same technique was used for the 2-D orbiter cross section for $\alpha = 60°$. A 3-D steady marching approach was used for the 3-D pointed nose orbiter shape for $\alpha = 40°$. The major advantage of this 3-D finite difference technique over other orbiter flowfield techniques[1–3] was its capability for treating bodies of arbitrary shape instead of being limited to analytically-defined body shapes. In this manner the shape of the fuselage can be specified in terms of a table of cross section contour point coordinates at various stations along the axis.[4]

These 2-D and 3-D finite difference methods were based on a modified Lax-Wendroff[24] scheme to solve the hyperbolic equations of the flowfield. The excessive undershoot and overshoot in flow properties occurring across a shock wave as computed by the original Lax-Wendroff scheme were minimized by means of a modified artificial viscosity technique. During the calculation the time-step size used between

Table 2 Test data compared with theory

Facility	Ref.	Type	α(°)	M_∞	Re_{∞_L}	H.T. data	Location	Press. data	Location
Ames 3.5ft hyper.W.T.	10	MSC st. wing orb.	40,60	7.4	9.6×10^6	.	Fuselage B.C.L.		
Ames 3.5ft hyper.W.T.	11	MSC st. wing orb.	40	7.4	1.1×10^6	.	Wing		
Ames 3.5ft hyper W.T.	12	NAR st. wing orb.	45	7.4	2.4×10^6			.	Fuselage B.C.L. & sides
Ames 42 in. shock tun.	13	MSC st. wing orb.	60	15	3×10^4	.	Fuselage B.C.L.		
Langley var. dens.W.T.	14	MSC st. wing orb.	60	8	3.8×10^6	.	Fuselage & wing		
Langley var. dens.W.T.	16	MSC st. wing orb.	60	8	3.8×10^6	.	Fuse. bottom & wing		
MSC 10 MW arc jet	14	MSC st. wing orb.	60	6	4×10^3	.	Fuselage B.C.L.		
MSC 10 MW arc jet	15	MSC st. wing orb.	60	10.4	5.7×10^3	.	Fuse. B.C.L. & side & wing		
LTV hyper.W.T.	17	MSC st. wing orb.	40,60	12,17	$2\text{–}4.5 \times 10^6$	.	Fuselage B.C.L. & wing	.	Fuselage B.C.L.
LTV hyper.W.T.	18	MSC st.wing orb.	60	15	4×10^6	.	Fuse. bottom		
Martin hot shot W.T.	17	MSC st. wing orb.	40	14	4.3×10^5	.	Wing		
CAL 6ft. hyper.S.T.	21	Flat plate	60	20	7.4×10^3	.	B.C.L. of plate	.	B.C.L. of plate
AEDC tunnel *B*	20	St. & del. body	40	8	2×10^6	.	Fuselage B.C.L.		
AEDC tunnel *B*	19	MDAC del. wing orb.	40	8	$4.5\text{–}6.6 \times 10^6$	.	Fuselage B.C.L.		
Grumman wind tunnel	22	GAEC del. wing orb.	40	10	6.8×10^5	.	Fuselage B.C.L.		

Note: B.C.L. = bottom center line.

successive grid planes was either input as a constant or was calculated by the program to satisfy the Courant-Friedericks-Levy stability conditions. A damping (dissipation) factor was input to control the numerical oscillations. As a result the flow variables were calculated as continuous functions in the shock regions and the shock had an arbitrary thickness of 2 or 3 space grids.

General Flow Equations

The system of conservative equations for compressible flow can be written in the following compact matrix notation

$$\{W_i\}_{,\alpha} = \{F_i\}_{,\beta} + \{G_i\}_{,\gamma} + Q_i \cdot \delta \tag{1}$$

where $\delta = 1$ for axisymmetric flow; otherwise $\delta = 0$. These vectors are functionally related as

$$F = F(W) \quad G = G(W) \quad Q = Q(W) \tag{2}$$

For inviscid 2-D time dependent flows, choose

$$\alpha = t,\ \beta = z,\ \gamma = r,\ \bar{\rho} = r^{\delta} \cdot \rho,\ \bar{p} = r^{\delta} \cdot p$$
$$\text{and} \quad \varepsilon = E + 1/2(u^2 + v^2) \quad \text{only} \tag{3}$$

The flow functions can then be written as

$$\{W_i\} = \begin{Bmatrix} \bar{\rho} \\ \bar{\rho}u \\ \bar{\rho}v \\ \bar{\rho}\varepsilon \end{Bmatrix}, \quad \{F_i\} = -\begin{Bmatrix} \bar{\rho}u \\ \bar{p} + \bar{\rho}u^2 \\ \bar{\rho}uv \\ u(\bar{\rho}\varepsilon + \bar{p}) \end{Bmatrix} \quad \text{and}$$

$$\{G_i\} = -\begin{Bmatrix} \bar{\rho}v \\ \bar{\rho}uv \\ \bar{p} + \bar{\rho}v^2 \\ v(\bar{\rho}\varepsilon + \bar{p}) \end{Bmatrix} \tag{4}$$

and

$$Q_1 = Q_2 = Q_4 = 0; \qquad Q_3 = p \cdot \delta \tag{5}$$

The equation of state is

$$\bar{p} = f(p, E) = (\gamma_{\text{eff}} - 1)\rho E \tag{6}$$

where γ_{eff} is 1.4 for an ideal gas. For real gases the effective value of γ was determined as a function of internal energy and density based on a curve fit of the equation of state[25] which was based on tabulated properties of air in equilibrium.[26]

For inviscid 3-D steady flows, the flow functions may be written as

$$\{W_i\} = \begin{Bmatrix} \rho u \\ p + \rho u^2 \\ \rho uv \\ \rho uw \end{Bmatrix}, \quad \{F_i\} = -\begin{Bmatrix} \rho v \\ \rho uv \\ p + \rho v^2 \\ \rho vw \end{Bmatrix} \quad \text{and}$$

$$\{G_i\} = -\begin{Bmatrix} \rho w \\ \rho uw \\ \rho vw \\ p + \rho w^2 \end{Bmatrix} \tag{7}$$

where in this representation of Eq. (1)

$$\alpha = x \quad \beta = y \quad \gamma = z \tag{8}$$

Finite Difference Solutions

The first order system of differential Eqs. (1) is hyperbolic, for which the initial value problem is well posed, This type of problem allows a marching procedure to be used starting from initial data. The flowfunctions are approximated in a Taylor series in the α variable with terms through the second order retained.[24] Defining $h = (\alpha,\beta,\gamma)$ as the coordinate vector, $h + \Delta\alpha = (\alpha + \Delta\alpha,\beta,\gamma)$, and considering that the first derivatives at the half step with respect to α are equivalent to derivatives of the vectors F and G with respect to β and γ, a Taylor series approximation to Eq. (1) for the full step may be written as

$$\{W_i\}^{h+\Delta\alpha} = \{W_i\}^{h} + \Delta\alpha \left[\{F_i\}_{,\beta}^{h+(\Delta\alpha/2)} + \{G_i\}_{,\gamma}^{h+(\Delta\alpha/2)} + Q_i^{h+(\Delta\alpha/2)} \cdot \delta/\Delta\alpha\right] + O(\Delta\alpha^3) \tag{9}$$

This expression in a finite difference form can be used to calculate the flowfunctions W_i at the coordinate $h + \Delta\alpha$ when the flow values are known at the coordinate h. In order to calculate the derivatives in (9), the values of the vectors F_i, G_i, and Q_i at the half-step may be calculated by using a Taylor series approximation of the functions W_i at the middle points.[4,7]

Introducing an additional dissipative mechanism controlled by the coefficient D_λ (where $D_\lambda \leq 1.0$), the final equation for the independent flow variables integrated at the full step becomes

$$W_i(h + \Delta\alpha) = D_\lambda W_i(h) + \left(\frac{D\lambda + 1}{2}\right)[\lambda_1 \overline{\Delta F_i} + \lambda_2 \overline{\Delta G_i}] - (D_\lambda - 1)(W1_i + W2_i + W3_i + W4_i) \tag{10}$$

where

$$\lambda_1 = \Delta\alpha/\Delta\beta,\ \lambda_2 = \Delta\alpha/\Delta\gamma,\ \overline{\Delta F_i} = F1_i - F2_i,\ \overline{\Delta G_i} = G3_i - G4_i \tag{11}$$

and the auxiliary functions $F1_i$, $F2_i$, $G3_i$, $G4_i$ at the middle step are determined from the functional relations

$$F1_i = f(W1_j),\ F2_i = f(W2_j),\ G3_i = f(W3_j), \quad \text{and} \quad G4_i = f(W4)_j \tag{12}$$

where the flow variables $W1_i$ etc., $W1_j$ etc., at the middle step are obtained using Taylor Expansions.[4]

When hyperbolic equations are solved numerically using an explicit scheme of computation, the maximum size of the marching step $\Delta\alpha$ is a function of the steps $\Delta\beta$,$\Delta\gamma$ along the other space variable and is limited by the Courant-Friedricks-Levy condition. In addition the particular scheme should satisfy the Von Neumann condition in order to expect numerically stable computations. The analysis of the stability condition using the linearized equations for this scheme results in the following maximum step size for 3-D steady flows

$$\Delta x \leq [\Delta l \Gamma/\tan(|\theta| + \mu)][D_\lambda/(D_\lambda + 1)]^{1/2} \tag{13}$$

in which Δl = smallest of Δy or Δz, $\Gamma \leq 1.0$, $D_\lambda \leq 1.0$, and $\theta = \arctan[(v^2 + w^2)^{1/2}/u]$.

For 2-D unsteady flows the stability condition which must be satisfied is

$$\Delta t \leq [\Delta x/(v + c)][D_\lambda/(D_\lambda + 1)]^{1/2} \tag{14}$$

where Δt is the time step.

Shock Layer Inviscid Flowfields

Since the 3-D steady finite difference analysis considered a slab wing (with sharp leading edge) attached to the body to keep the entire flowfield supersonic, another flowfield method was used for the subsonic flow around the leading edge of the actual airfoil of the orbiter wing. Although the 2-D time-dependent finite difference method could have been used at various span locations for this airfoil analysis, the number of locations required to obtain correlation with heat transfer data dictated that a faster and more economical technique be used. The TRW shock layer analysis program, an inverse problem solution technique, was thus employed, using the 3-D finite difference results immediately upstream of the wing leading edge.

The Shock Layer Analysis Program calculates the subsonic and low supersonic ($M_1 \approx 1.5$) flowfield behind a shock in front of a generalized 2-D planar blunt-nosed body (e.g., airfoil at large α) or a 3-D axisymmetric blunt-nosed body at $\alpha = 0$ in hypersonic flow.[27] The complete inviscid flowfield behind the shock including surface pressure is calculated

both upstream and downstream of the stagnation point as a function of the distance from the shock to the body.

In addition to using the output from the 3-D finite difference program at $\alpha = 40°$, the shock layer program also used the 2-D finite difference results for the orbiter fuselage cross section at $\alpha = 60°$. For this case a simulated wing was attached to the chine line of the cross section at a dihedral angle of 7°, and the flowfield around several airfoils was computed using the shock layer program. For the $\alpha = 60°$ case, the assumption was made that the velocity parallel to the bottom of the fuselage was equal to $v_\infty \cos\alpha$. The other velocity components were taken from the 2-D finite difference results at selected locations along the span.

Boundary-layer Flow and Heating Rates

After the inviscid flowfields around the various orbiter shapes were obtained, the viscous boundary-layer flow and heating rates were determined. In previous orbiter re-entry heating studies various simplified laminar flow theories have been used to predict heating to the fuselage windward centerline and wing leading edges. These have included cross flow theory,[10] swept cylinder theory,[13,17,18] tangent cone theory,[17,18] tangent wedge theory,[18,22] local similarity,[28] and the "rho-mu" theory.[29] Among the turbulent theories used for the orbiter fuselage centerline are the strip theory accounting for flow divergence,[10] integral method of Van Driest,[20] Spalding, and Chi's method,[10,19,20] and a modification of the integral method of Reshotko and Tucker.[28]

In the present analysis the heating rates on the orbiter surfaces for both laminar and turbulent flow were computed by a nonsimilar, multicomponent boundary-layer integral matrix program (BLIMP).[30] This program which includes the effects of chemical reactions, foreign gas injection, ionization, and entropy gradients, obtains nonsimilar solutions by using implicit quadratic finite difference terms applied to the streamline derivatives. In a comprehensive review of the literature this program was recently shown to be one of the best available nonsimilar boundary-layer programs for shuttle orbiter re-entry heating applications.[31]

For the configurations analyzed in this study the finite difference or shock layer inviscid flow pressure distributions along the surface were used as input to the BLIMP program along with the stagnation pressure, stagnation enthalpy, and the equilibrium air species concentrations. The assumption of a planar sharp body was made for the flat plate cases, a planar blunt body was considered for the 2-D orbiter fuselage cross sections and wing airfoils, and an axisymmetric sharp body using the radial distance from the fuselage axis to the chine line as the local body radius was used for the 3-D orbiter geometry.

Results

The sonic lines, shock waves, and stagnation points as calculated by the 2-D time-dependent finite difference method for a 1.5 ft long flat plate at $\alpha = 60°$ tested in the CAL 6 ft Hypersonic Shock Tunnel[21] are shown in Fig. 1. For this angle of attack it may be seen that subsonic flow exists along the entire plate length (and similarly along the entire orbiter underside). The stagnation point lies closer to the leading edge for the real gas case than for the ideal gas case, resulting in steeper pressure and velocity gradients, and, hence, higher heating rates in the stagnation region. Also the shock wave and sonic line are closer to the plate for the real gas case than for the ideal gas case. The corresponding heating rate coefficients, C_H, computed for these inviscid flowfields are shown in Fig. 2 along with the CAL[21] data. It may be seen that the heating rate predictions for a real gas show excellent correlation with the data and are higher than the calculations

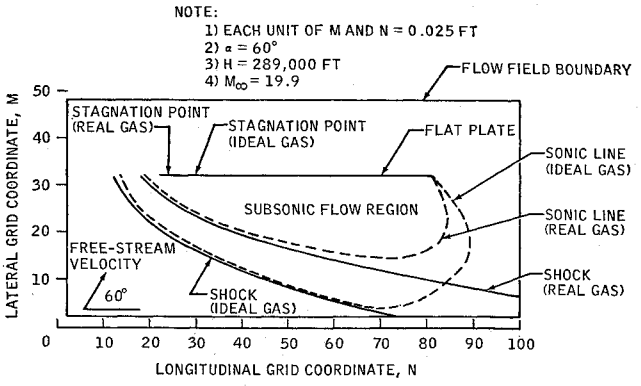

Fig. 1 Flowfield mesh, sonic lines, and shocks for flat plate computed by 2-D time-dependent finite difference method.

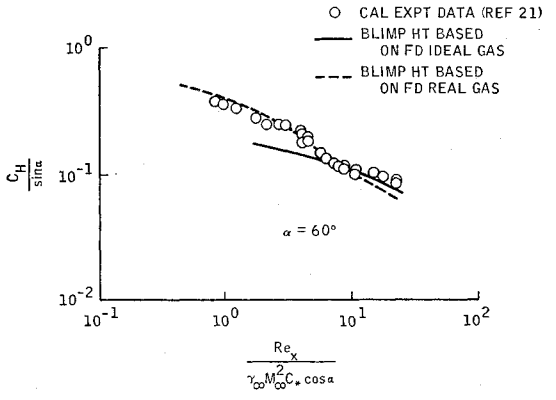

Fig. 2 Heat transfer comparison on a flat plate with data.

for an ideal gas because of the location of the stagnation point (Fig. 1).

In Fig. 3 seven sets of laminar flow heat transfer data for the centerline of the underside of the orbiter fuselage at $\alpha = 60°$ are shown in comparison with the predicted heat transfer rate. The 2-D time-dependent finite difference real gas flowfield was used as input to the BLIMP program for a 120 ft long flat plate at $\alpha = 60°$, representing the flat underside of the orbiter. The 2-D flat plate (planar sharp body) heating rates were corrected for 3-D effects (conical flow) by multiplying them by $3^{1/2}$. Although there are more accurate means of including 3-D effects, such as the inviscid surface streamline/local similarity method[28] and the BLIMP program[30] used for the $\alpha = 40°$ case (discussed later), there was excellent agreement with the data for about the first 2/3 of the plate using this analysis.

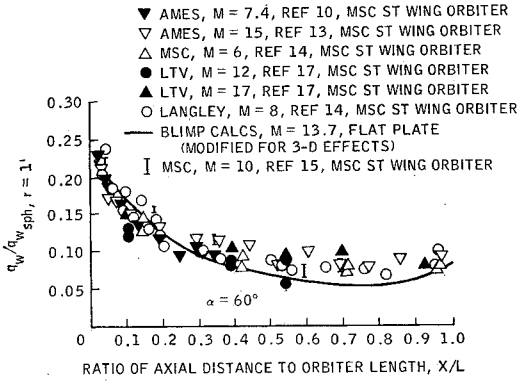

Fig. 3 Laminar heating rates on underside of orbiter.

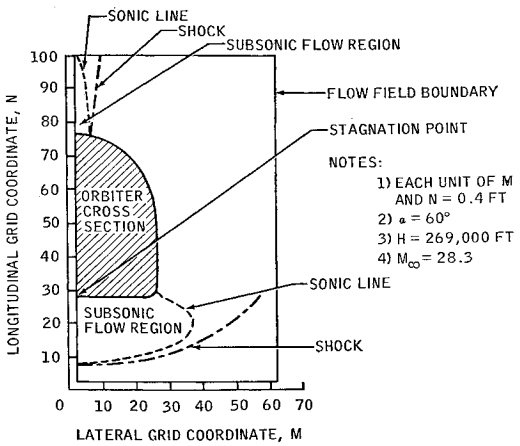

Fig. 4 Flowfield mesh, sonic line, and shock wave for orbiter cross section computed by 2-D time dependent finite difference method.

The flowfield and shock structure around the orbiter cross section for $\alpha = 60°$ as computed by the 2-D time-dependent finite difference method for an ideal gas are seen in Fig. 4. There is a large subsonic region in the vicinity of the stagnation point and a smaller subsonic region at the top of the cross section (which for an actual orbiter will be separated). The pressure distribution around this cross section from the bottom centerline to the top (outside of the shock) varied by some three orders of magnitude and the heating rates by some two orders of magnitude. The heating rate predictions (normalized by the centerline value) along the front face are presented in Fig. 5 along with experimental data,[16,18] showing the increase near the chine line as the flow accelerates in this region. There is reasonably good agreement with the data, with the calculations at the chine line being somewhat higher than the data because of the corner radius/base radius ratio being lower for the calculations (0.0833) than for the test model (0.12).

The results of the 2-D time-dependent finite difference flow field calculations for the orbiter cross section at $\alpha = 60°$ (Fig. 4) were also used with the Shock Layer and BLIMP Programs to obtain the flowfield and heating rates around several airfoils near the shock intersection region. The heating rate predictions on the airfoils near the wing leading edge normalized by the freestream values at large span lengths are shown in Fig. 6 compared to data[11,15,16] for straight

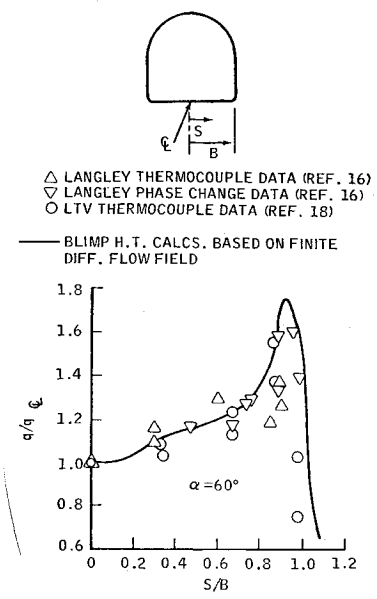

Fig. 5 Heating rates around orbiter cross section.

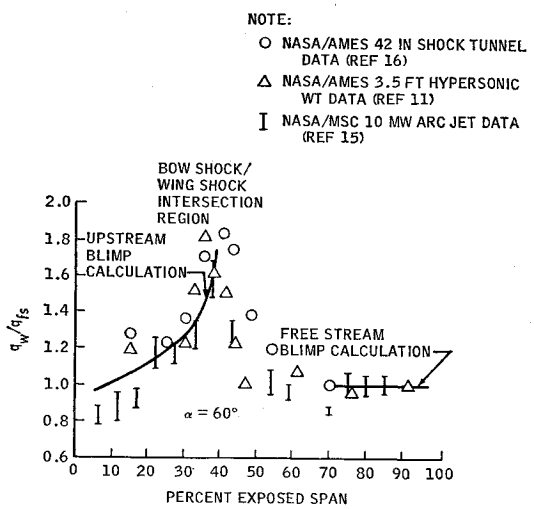

Fig. 6 Heating rates on leading edge of orbiter wing.

wing orbiters at $\alpha = 60°$. Reasonably good correlation was obtained with the data on the inboard side of the shock, showing the shock intersection region to occur at approximately 35–40% of the exposed span. No calculations were made on the outboard side of the shock since the 2-D finite difference results did not extend this far; however, a freestream calculation which is shown for the undisturbed region is in good agreement with the data.

For the 3-D representations of the orbiter, a pointed cone of 26.5° half-angle, inclined at 11.5° to the horizontal was used for the front of the fuselage. The 3-D steady finite difference calculations for the conical nose were carried out to about 4.4 ft where the cone gradually tapered into the fuselage of variable cross section as seen in Fig. 7. The conical flow results were used as inputs for the downstream calculations. The shock waves at various axial stations of varying and constant cross section are seen in Fig. 7. At about 70.6 ft from the nose, the wing leading edge was reached and the attached shock around the wing was calculated.

The resultant 3-D finite difference surface pressure predictions along the bottom centerline of the orbiter are compared with data[12] for a straight wing orbiter in Fig. 8. Reasonably good agreement exists between the theory for $\alpha = 40°$ and data at $\alpha = 45°$. Also shown on this figure

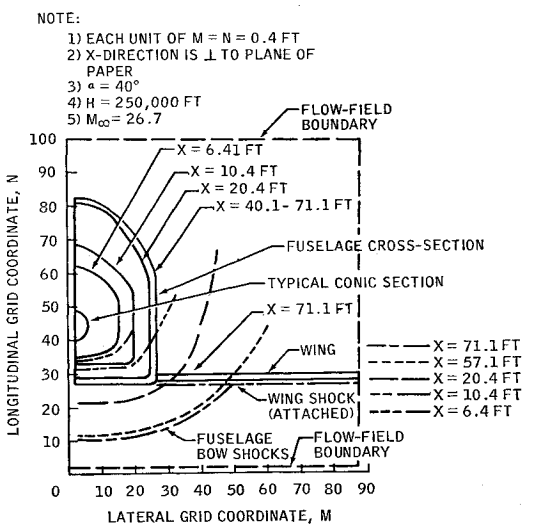

Fig. 7 3-D orbiter fuselage cross sections and shocks computed by 3-D steady finite difference method.

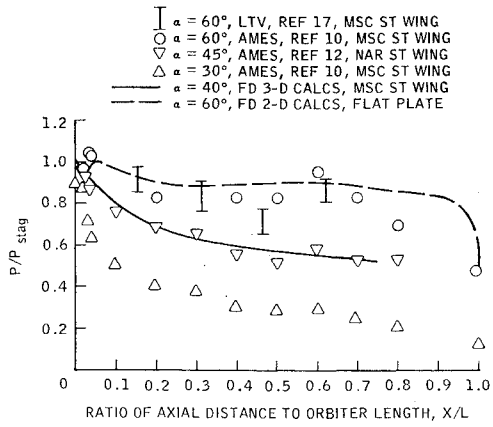

Fig. 8 Pressures on underside of orbiter fuselage.

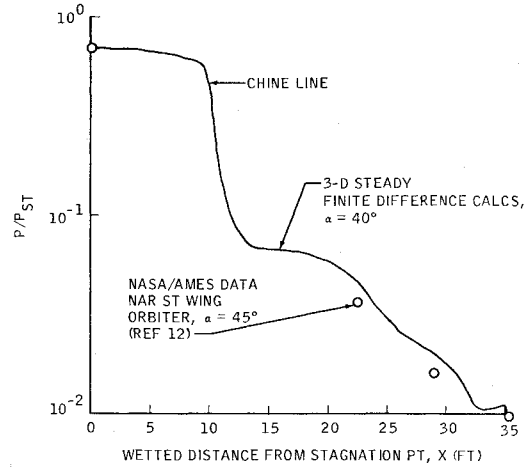

Fig. 10 Pressures around cross section of orbiter fuselage at $X/L = 0.2$.

are the 2-D time-dependent finite difference pressure predictions for a flat plate at $\alpha = 60°$ compared with straight wing orbiter data[10] at $\alpha = 60°$. Fairly good agreement with this data exists for the flat plate model except slightly upstream of the trailing edge.

In Fig. 9 the laminar and turbulent heating rate predictions on the underside of the 3-D orbiter fuselage at $\alpha = 40°$, based on calculated inviscid pressures, are compared with numerous orbiter experimental data. Excellent agreement resulted with the laminar and turbulent data[10] for a straight wing orbiter at $\alpha = 40°$. Reasonably good agreement existed for the other data; although the delta wing orbiter data[19, 22] was slightly higher than the laminar calculations (which were based on the straight-wing orbiter).

At the station $x/L = 0.2$ on the 3-D body, the surface pressures around the body computed by the 3-D steady finite difference method at $\alpha = 40°$ are shown in Fig. 10 compared with data [12] for a straightwing orbiter at $\alpha = 45°$. Good agreement in the lateral direction between theory and data resulted at this station and at several other axial stations not shown.

Figure 11 shows the predicted spanwise heating rates near the leading edge of the orbiter wing for $\alpha = 40°$ compared with data[11] for $\alpha = 40°$. For this analysis the 3-D steady finite difference flow properties just upstream of the wing were used as input to the shock layer program. Twelve airfoil sections along the span were used to obtain the resultant surface pressure distribution which was then input to the BLIMP program to obtain the heating rate distribution around each airfoil. The stagnation point values (at roughly 3–5% of the cord) along the span are presented in the figure which shows very good agreement with the data except at the highest data point which is believed to be due to a boundary-layer/shock interaction phenomena corresponding to Edney's Type V model.[32] The bow shock/wing shock intersection point occurs about 37–38% of the exposed span which is at about the same location as shown[17] for straight-wing orbiter data for $\alpha = 40°$.

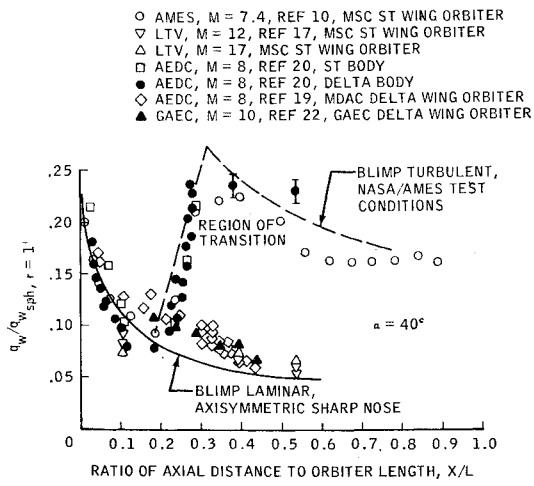

Fig. 9 Heating rates on underside of orbiter fuselage.

Conclusion

An analysis of the inviscid and boundary-layer flowfields and heating rates in the continuum flow regime was performed for a straight-wing shuttle orbiter at angles of attack of 40° and 60°. The finite difference 2-D time-dependent and 3-D steady methods were used to predict more accurately the flows behind detached and attached shocks, respectively, because of the modified artificial viscosity approach which allowed smoother properties across the shock waves. These finite difference methods, together with the shock layer and heating analysis for the airfoils enabled the fuselage bow shock/wing shock intersection region to be determined with a good degree of accuracy. The finite difference pressure predictions and the heating rate predictions for the windward portion of the fuselage at both $\alpha = 40°$ and 60° showed good agreement with the experimental data. Two of the authors of this paper, d'Attorre and Bilyk, are currently applying the same finite difference techniques to the flowfield around a high performance swing wing/delta type of aircraft.[33] It is thus believed that the analytical methods described herein can be

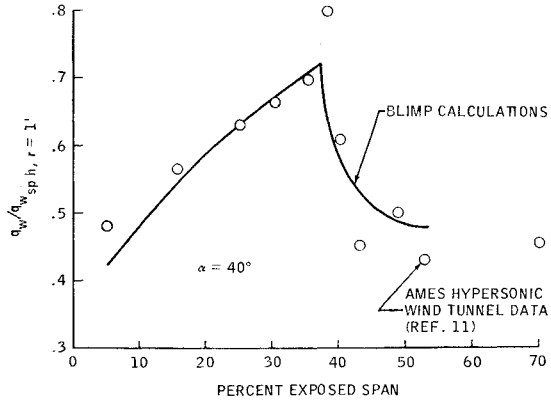

Fig. 11 Heating rates on leading edge of orbiter wing.

used satisfactorily for design studies on the current delta wing space shuttle orbiter and other supersonic and hypersonic aircraft at high angle of attack.

References

[1] "Space Shuttle Aerothermodynamics Technology Conference Vol. I—Flow Fields," TM X-2506, Feb. 1972, NASA.

[2] "NASA Space Shuttle Technology Conference. Vol. I—Aerothermodynamics, Configurations, and Flight Mechanics," TM X-2272, April 1971, NASA.

[3] "Space Transportation System Technology Symposium. Vol. I —Aerothermodynamics and Configurations," TM X-52876, July 1970, NASA.

[4] Rochelle, W. C. et al., "Space Shuttle Vehicle Reenetry Flow-Field Analysis—Final Report," Rept. 16209-H002-R0-00, July 1971, TRW Systems, Houston, Texas.

[5] Vogenitz, F. W. et al., "Monte Carlo Direct Simulation Technique—User's Manual," Rept. 16209-H001-R0-00, July 1971, TRW Systems, Redondo Beach, Calif.

[6] Rochelle, W. C., Roberts, B. B., Vogenitz, F. W., and d'Attorre, L., "Space Shuttle Orbiter Reentry Flow Field and Heating Analysis," TM X-2506, Feb. 1972, NASA.

[7] Rochelle, W. C., Roberts, B. B., d'Attorre, L., and Vogenitz, F. W., "Reentry Heating and Flow Fields for Space Shuttle Orbiter at High Angle of Attack," AIAA Paper 72-314, San Antonio, Texas, 1972.

[8] Garcia, F., "Nominal Reentry Trajectory for the April Baseline Space Shuttle Vehicle," Memo EX24/7003-10903, March 1970, NASA/MSC.

[9] Gomez, A. V., "Task 701—Wing Leading Edge TPS Weight Study, Progress Report No. 1," Rept. 70.4352.30-6, June 1970, TRW Systems, Houston, Texas.

[10] Marvin, J. G., et al. "Flow Fields and Aerodynamic Heating of Space Shuttle Orbiter," TM X-2272, April 1971, NASA.

[11] Seegmiller, H. L., "Shock Interference Heating and Density Ratio Effects: Part I—Flow Field Visualization, Thermocouple Measurements, and Analysis," TM X-2272, April 1971, NASA.

[12] Pappas, C. C., unpublished experimental orbiter pressure data obtained in NASA/Ames 3.5 ft. hypersonic shock tunnel, transmitted to W. C. Rochelle, May, 1971.

[13] Pappas, C. C., "The Calculation of Laminar Heat Transfer to the Windward Surfaces of the MSC Orbiter at High Angle of Attack and with Yaw," TN, 1973, NASA.

[14] Lee, D. B., "Aerothermodynamic Data on MSC Space Shuttle," Memo ES5/7-10(0)/163(m), July 1970, NASA/MSC.

[15] Scott, C. D., "Heating Rates to Wing Leading Edge and Fuselage Chine Line Obtained on a 1/80 Scale Model of the Shuttle Orbiter Tested in the MSC 10 Mw Arc Tunnel Facility," Memo from Thermal Technology Branch, Dec. 1970, NASA/MSC.

[16] Katzen, E. D., "Static Aerodynamics, Flow Fields, and Aerodynamic Heating of Space Shuttle Orbiters," TM X-52876, July 1970, NASA.

[17] Bertin, J. J. et al., "Aerothermodynamic Measurements for Space Shuttle Configurations in Hypersonic Wind Tunnels," Aerospace Engineering Rept. 71006, Sept. 1971, Univ. of Texas, Austin, Texas.

[18] Bertin, J. J. et al., "Flow Field Measurements for Cylindrical Configurations in a Hypersonic Wind Tunnel: Windward and Leeward Flow Fields," Aerospace Engineering Rept. 71007, Dec. 1971, Univ. of Texas, Austin, Texas.

[19] Matthews, R. K. et al., "Experimental and Theoretical Aerodynamic Heating and Flow Field Analysis of a Space Shuttle Orbiter," TM X-2507, Feb. 1972, NASA.

[20] Johnson, C. B., "High Reynolds No. Turbulent Heating to Two Simplified Shuttle Configurations," TM X-2507, Feb. 1972, NASA.

[21] Vidal, R. J. and Bartz, J. A., "Experimental Studies of Low-Density Effects in Hypersonic Wedge Flows," *Rarefied Gas Dynamics*, Vol. 1, Academic Press, New York, 1965.

[22] Mendelsohn, A. R., "A Review of the Grumman Orbiter Wind Tunnel Heat Transfer Tests," TM X-2507, Feb. 1972, NASA.

[23] Adams, J. C. and Martindale, W. R., "Hypersonic Lifting Body Windward Surface Flow-Field Analysis for High Angles of Incidence," AEDC-TR-73-2, Feb., 1973, Arnold Engineering Development Center, Tullahoma, Tenn.

[24] Lax, P. D. and Wendroff, B., "Difference Schemes for Hyperbolic Equations with High Order of Accuracy," *Communications on Pure and Applied Mathematics*, Vol. 17, 1964, pp. 381–398.

[25] Doan, L. R. and Nickel, G. H., "A Subroutine for the Equation of State of Air," AFWL TM-RTD (WLR) TM-63-2, 1963, Air Force Weapons Laboratory, White Sands, N. Mex.

[26] Hilsenrath, J. and Beckett, C. W., "Tables of Thermodynamic Properties of Argon-Free Air to 15,000 °K," AEDC TN 56-12, 1956, Arnold Engineering Development Center, Tullahoma, Tenn.

[27] Gomez, A. V., "Hypersonic-Blunt Body, Shock Layer Analysis Program (AH002A)," Rept. 70.4352.30.02, May 1970, TRW Systems, Houston, Texas.

[28] Hamilton, H. H. and de Jarnette, F. R., "Inviscid-Surface-Streamline Program for Use in Predicting Shuttle Heating Rates," TM X-2506, Feb. 1972, NASA.

[29] Guard, F. L. and Schultz, H. D., "Space Shuttle Aerodynamic Heating Considerations," ASME Paper 70-HT/SpT-16, presented at ASME Space Technology and Heat Transfer Conference, June, 1970, Los Angeles, Calif.

[30] Bartlett, E. P., "User's Manual—Boundary Layer Integral Matrix Procedure, Version C." Rept. UM-70-20, June 1970, Aerotherm Corp., Mountain View, Calif.

[31] Bartlett, E. P., Morse, H. L., and Tong, H., "Investigation of Thermal Protection Systems Effects on Viscid and Inviscid Flow Fields for Manned Entry Systems," Rept. 71-38, Sept. 1971. Aerotherm Corp., Mountain View, Calif.

[32] Edney, B. E., "Shock Interference Heating and the Space Shuttle," TM X-52876, July 1970, NASA.

[33] D'Attorre, L. and Bilyk, M. A., "Three Dimensional Inviscid Flow Field Analysis-Forebody of an Air-Vehicle," TRW Rept. 22945-6001-R0-00, Aug. 1972, TRW Systems, Redondo Beach, Calif.